Factors Regulating the Multidecadal Changes in MJO Amplitude over the Twentieth Century

ZHEN FU, PANG-CHI HSU, AND FEI LIU

Key Laboratory of Meteorological Disaster of Ministry of Education/Joint International Research Laboratory of Climate and Environment Change/Collaborative Innovation Center on Forecast and Evaluation of Meteorological Disasters, Nanjing University of Information Science and Technology, Nanjing, China

(Manuscript received 17 February 2020, in final form 6 July 2020)

ABSTRACT: This study examined multidecadal changes in the amplitude of the boreal-winter Madden–Julian oscillation (MJO) over the twentieth century using two century-long reanalysis datasets (20CR and ERA-20C). Both revealed reasonable MJO variability compared to other state-of-the-art reanalysis datasets. We detected pronounced multidecadal variations along with an increasing trend in MJO amplitude during the period 1900–2009 in both datasets, although this linear trend was less significant in the reconstructed MJO index proposed by Oliver and Thompson. The two twentieth-century reanalysis datasets and the Oliver–Thompson MJO index consistently showed the intensified amplitude of MJO precipitation and circulation in the later decades (1970–99) compared to the earlier decades (1920–49). The most significant enhancement of MJO precipitation in the later decades appeared over the western Pacific warm pool. To understand the mechanisms controlling the changes in western Pacific MJO precipitation amplitude over the twentieth century, we diagnosed the moisture budget equation. The enhanced MJO precipitation variability in the later decades mainly came from increased moisture associated with a strengthened low-level convergence anomaly working on background mean moisture $[-(\overline{q}\nabla \cdot V')]$. Further diagnosis showed that the effect of anomalous circulation $(\nabla \cdot V')$ change on the MJO precipitation amplitude change over the twentieth century was about an order larger than that of mean moisture $(\overline{q})$ change, different from the mechanisms (i.e., increased gradient of $\overline{q}$) responsible for the intensified MJO precipitation amplitude under future warmer climate. The enhanced MJO circulation anomalies during 1970–99 may be caused by an enhanced diabatic heating anomaly, offset partly by the increased mean static stability.

KEYWORDS: Madden-Julian oscillation; Moisture/moisture budget; Intraseasonal variability; Multidecadal variability

1. Introduction

The Madden–Julian oscillation (MJO), a planetary-scale atmospheric circulation anomaly coupled with deep convection, is the dominant mode of intraseasonal variability over the tropics (Madden and Julian 1971, 1972). The MJO convection is generally initiated in the western equatorial Indian Ocean and strengthens as it propagates eastward through the Indo-Pacific warm-pool regions. The convection of the MJO is weakened significantly after arriving over the cold tongue region (Zhang 2005). Numerous studies have documented the influences of the MJO on different weather and climate systems over the globe, such as the global monsoons (Goswami and Mohan 2001; Lorenz and Hartmann 2006; Pohl et al. 2009), tropical cyclones (Camargo et al. 2009), El Niño–Southern Oscillation (ENSO; Lengaigne et al. 2004; Zavala-Garay et al. 2005), and other tropical and extratropical extreme events (Carvalho et al. 2004; Lin et al. 2010). Unfortunately, accurate simulation and prediction of the MJO and its impacts are still challenging (Vitart and Molteni 2010; Fu et al. 2013; Klingaman et al. 2015; Ling et al. 2019), partially due to our incomplete understanding of the MJO dynamics (Kim et al. 2011; Zhang et al. 2013; Jiang et al. 2015).

The MJO intensity (i.e., the amplitude of MJO variability) varies at different time scales, including the seasonal cycle (Salby et al. 1994; Zhang and Dong 2004), interannual (Madden and Julian 1994; Hendon et al. 1998; Slingo et al. 1999; Kessler 2001; Chen et al. 2016; Hsu and Xiao 2017), and decadal scales (Slingo et al. 1999; Jones and Carvalho 2006), as well as with the long-term change associated with anthropogenic warming (Liu et al. 2013; Subramanian et al. 2014; Arnold et al. 2015; Chang et al. 2015; Adames et al. 2017; Wolding et al. 2017; Bui and Maloney 2018; Cui and Li 2019; Maloney et al. 2019; Rushley et al. 2019). The mechanisms responsible for the MJO intensity are generally linked to background thermodynamic conditions. For example, the meridional movement of active MJO locations in a year is consistent with the annual cycle of sea surface temperature (SST) centers and low-level moisture convergence regions (Salby et al. 1994; Zhang and Dong 2004). The spatial extents of warm SST influenced by the ENSO lead to anomalous moisture and large-scale circulations over the Indo-Pacific warm-pool region where the MJO is vigorous. As a result, the enhanced MJO signals tend to extend farther east toward the central-eastern Pacific (confined to the western Pacific) during warm (cold) ENSO years (Hendon et al. 1998; Kessler 2001; Zhang 2005). The complexity of SST patterns associated with different ENSO types also affects the MJO intensity during its initiation and propagating stages through modulating the background conditions and scale interaction processes (Chen et al. 2016; Hsu and Xiao 2017). The changes in SST pattern under global warming can also exert profound influences on changes in MJO characteristics (Maloney and Xie 2013; Cui and Li 2019). A recent paper of Roxy et al. (2019) suggested that the expansion of western Pacific warm pool would lead to a longer persistence of western Pacific MJO.

Corresponding author: Pang-Chi Hsu, pangchi@nuist.edu.cn

DOI: 10.1175/JCLI-D-20-0111.1

The decadal-to-multidecadal variation of the MJO intensity has received less attention owing to limited observations. An early study of Slingo et al. (1999) assessed the MJO's behavior during 1958–97 using the National Centers for Environmental Prediction (NCEP) Reanalysis 1 dataset; they found that the amplitude of MJO wind field at 200 hPa in 1958–76 was weaker than that in 1977–96. To verify whether this finding resulted from the improvement of reanalysis quality during the satellite era, Slingo et al. (1999) conducted a model simulation forced by observed SST in 1949–93. The simulated MJO reproduced the positive trend in observed MJO amplitude, confirming the influences of SST warming over the second half of the twentieth century on the intensified MJO activity. Similarly, Jones and Carvalho (2006) used the NCEP reanalysis data to investigate the variation in the strength of MJO zonal winds in the lower and upper troposphere over the period 1958–2004. Positive linear trends were identified in the amplitude of MJO zonal winds during both boreal summer and winter seasons.

Besides reanalysis-based studies (Slingo et al. 1999; Jones and Carvalho 2006), a number of studies have discussed the impact of anthropogenic warming on MJO amplitude using either single model simulations (Subramanian et al. 2014; Arnold et al. 2015; Chang et al. 2015; Adames et al. 2017; Wolding et al. 2017) or model outputs of phase 5 of the Coupled Model Intercomparison Project (CMIP5) (Bui and Maloney 2018; Maloney et al. 2019; Rushley et al. 2019). Nearly all of the models project enhanced variability of MJO precipitation in a warmer future climate (Maloney et al. 2019), which can be related to increased background moisture (Chang et al. 2015; Wolding et al. 2017; Bui and Maloney 2018) and enhanced variability of background tropical precipitation (Adames et al. 2017; Rushley et al. 2019). However, the changes in MJO wind variability under anthropogenic warming have large uncertainty. Some models show a small increase in the variability of MJO circulation, while others project weakened MJO wind variability (Adames et al. 2017; Wolding et al. 2017; Bui and Maloney 2018). The relatively small increase or even decrease in the amplitude of MJO circulation under global warming might be caused by the increased static stability over the tropics (Maloney et al. 2019). The decreased strength of MJO circulation would further result in a weakened MJO teleconnection over the middle and high latitudes (Wolding et al. 2017).

Although the enhancement of MJO precipitation variability under warming climate is a consensus from studies using both reanalysis data and model projections, the changes in MJO circulation variability show diverse results, with a clear increasing trend over the second half of the twentieth century (Slingo et al. 1999; Jones and Carvalho 2006), but a moderate increase or decrease in model simulations (Adames et al. 2017; Wolding et al. 2017; Bui and Maloney 2018). Bui and Maloney (2019a) also emphasized the uncertainty of changes in MJO precipitation and circulation induced by global warming in the CMIP5 projections. Most of these modeling studies suggest that anthropogenic climate change would induce a higher stability, which weakens the amplitude of MJO circulation, but the cause of the intensified MJO wind variability from the 1960s to 2000 remains unclear. Observational studies (Slingo et al. 1999; Jones and Carvalho 2006) did not explain the long-term changes in MJO precipitation variability under current global warming, which is also worthy of discussion and comparison with future projections.

Benefitting from modern reanalysis systems, the aim of this study is to quantitatively examine the changes in MJO precipitation and wind amplitude and their associated mechanisms responsible for these changes over the entire twentieth century using two century-long reanalysis datasets—one from the United States and one from Europe. To obtain more reliable and robust results, the basic MJO features derived from the twentieth-century reanalysis datasets were first compared with several other state-of-the-art reanalysis datasets and the reconstructed MJO index proposed by Oliver and Thompson (2012). We selected the epochs with consistent increased and decreased MJO variability for further diagnosis to understand the mechanisms regulating MJO amplitude, similar to the approaches used by some modeling studies.

The rest of this paper is organized as follows. The data and methods used in the study are introduced in section 2. In section 3, we present the basic MJO behaviors in the two twentieth-century reanalysis datasets and compare them with those derived from other commonly used reanalysis datasets. In section 4, we identify the long-term changes in MJO precipitation and wind variability over the twentieth century using the long-term observations from the twentieth-century reanalysis datasets, NCEP-1 reanalysis, and the reconstructed MJO index proposed by Oliver and Thompson (2012). Then, the moisture and dry static energy (DSE) budget equations are diagnosed to understand the key processes causing the multidecadal changes in MJO precipitation and circulation amplitude, with a focus on the relative effects of thermodynamic and dynamic conditions at different time scales. In section 5, we further examine the factors regulating the amplitude of circulation anomaly changes. A summary is given in section 6.

2. Data and methods

a. Data

Two century-long reanalysis datasets are used in this study to investigate the MJO activity from the beginning of the twentieth century to the present (1900–2010). One is the Twentieth Century Reanalysis version V2c (20CR; Compo et al. 2011) from the National Oceanic and Atmospheric Administration (NOAA); the other is the European Centre for Medium-Range Weather Forecasts (ECMWF) first atmospheric reanalysis of the twentieth century (ERA-20C; Poli et al. 2016). These two datasets provide long (>100 years) and gap-free three-dimensional meteorological variables, including zonal and meridional (u and v) wind components, vertical pressure velocity ω, specific humidity q, and geopotential height z fields from 1000 to 100 hPa. Variables related to convective activity, such as outgoing longwave radiation (OLR) and precipitation, are also provided. Considering the data spread from ensemble members of 20CR, we used both the ensemble mean of 56 members and individual members to analyze the MJO activity in 20CR. Different from 20CR, ERA-20C is a deterministic (i.e., single member) product,

although it uses a 10-member ensemble for background error estimations.

While these two twentieth-century reanalysis systems assimilate only the surface information using modern data assimilations, they do include the basic characteristics of the MJO (see section 3) and display decadal variation in MJO amplitude that is consistent with other long-term datasets (see section 4). Note that the aim of this study is not to present an accurate estimate of observed variation in the MJO, which has been documented in many studies based on reanalysis datasets with assimilation of improved observational data after 1979. Instead, our intention is to reveal the decadal-to-multidecadal variations of MJO amplitude from the last century to the present day, an issue that has received very little attention. The complete sets of climate variables provided by 20CR and ERA-20C are useful for diagnostic work that helps us understand the mechanisms regulating the intensity changes in MJO precipitation and circulation at the multidecadal time scale.

To demonstrate the feasibility of the twentieth-century reanalysis datasets in revealing the behaviors of the MJO, the following datasets covering the period 1979–2010 were also selected: 1) The NCEP–U.S. Department of Energy Reanalysis II (NCEP-2; Kanamitsu et al. 2002), 2) the NCEP Climate Forecast System Reanalysis (CFSR; Saha et al. 2010), 3) the ECMWF Interim Reanalysis (ERA-Interim; Dee et al. 2011), and 4) the Modern-Era Retrospective Analysis for Research and Applications (MERRA; Rienecker et al. 2011). Longer data records from the NCEP Reanalysis-I (NCEP-1; Kalnay et al. 1996) during 1948–2010 and Oliver and Thompson's (2012) reconstructed MJO index over the period 1905–2014 were also used. This historical reconstruction of the MJO index (I^{HR}) was generated by multiple linear regression of surface pressure time series at 12 locations onto the real-time multivariate MJO (RMM) index proposed by Wheeler and Hendon (2004) based on the 20CR dataset. We obtained the updated I^{HR}, which contains the date, MJO amplitude, and MJO phase during 1905–2014 (http://passage.phys.ocean.dal.ca/~olivere/histmjo.html).

Other observational data include daily OLR from NOAA (Liebmann and Smith 1996), observed SST from the Simple Ocean Data Assimilation with Sparse Input (SODAsi) version 2 (SODAsi.2; Giese et al. 2016), and the Hadley Center Sea Ice and Surface Temperature dataset (HadISST) version 2.1 (Titchner and Rayner 2014). SODAsi.2 and HadISST2.1 were used as the boundary conditions for the 20CR and ERA-20C atmospheric reanalysis models, respectively.

To unify the spatial resolutions of different datasets, all the data were interpolated into 2.5° × 2.5° grid. We focused on the boreal winter season (November–April), when the MJO signal is most evident.

b. Definitions of MJO phase and amplitude

Similar to Wheeler and Hendon (2004) and Waliser et al. (2009), the MJO phase evolution and amplitude are defined based on the multivariate EOF (MEOF) analysis for 20–90-day-filtered 850-hPa zonal wind (U850), 200-hPa zonal wind (U200), and OLR. The variability of the first two principal components (PC1 and PC2) is used to define the MJO amplitude, namely, $(PC1^2 + PC2^2)^{1/2}$. Note that the Lanczos bandpass filtering (Duchon 1979) is applied in this study to extract the MJO-related components instead of using the running mean-based method for deriving the real-time multivariate MJO (RMM) index as proposed by Wheeler and Hendon (2004). The 20–90-day bandpass filtering retains only the signals associated with intraseasonal oscillation, while the RMM index contains partly the background low-frequency signals, leading to some uncertainty of long-term MJO trend detected by the RMM index (Lyu et al. 2019).

c. Moisture and DSE budget diagnoses

To understand the source of moisture, which is closely linked to precipitation, the budget equation of moisture perturbation (Yanai et al. 1973) was diagnosed:

$$\frac{\partial q'}{\partial t} = -(V \cdot \nabla q)' - (q\nabla \cdot V)' - \frac{\partial}{\partial p}(\omega q)' - \frac{Q_2'}{L}, \tag{1}$$

where the primes denote the 20–90-day component, V is the horizontal wind field, ∇ is the horizontal gradient operator, p is pressure, L is the latent heat of condensation, and Q_2 is the apparent moisture sink as the residual of the moisture budget (Yanai et al. 1973). Thus, the terms on the right-hand side of Eq. (1) present the horizontal advection of moisture, horizontal moisture convergence, vertical flux term of moisture, and moisture gain or loss, respectively, at the MJO time scale (i.e., 20–90 days).

The apparent heat source Q_1 associated with the MJO can be derived using the DSE budget equation (Yanai et al. 1973):

$$\left(\frac{\partial s}{\partial t}\right)' + (V \cdot \nabla s)' + \left(\omega \frac{\partial s}{\partial p}\right)' = Q_1', \tag{2}$$

where s denotes the DSE ($s = C_pT + gz$, where T is temperature, C_p is the specific heat of dry air at constant pressure, g is gravity, and z is the geopotential height). According to Eq. (2), the apparent heat source (including diabatic heating and eddy flux convergence of the subgrid DSE process) is modulated by the DSE tendency and the horizontal and vertical advections of DSE. With the assumption of a weak temperature gradient in the tropics, the tendency and horizontal advection of DSE are negligible (Sobel et al. 2001). Thus, the vertical motion of MJO ω' is largely regulated by MJO-related diabatic heating Q_1' and the time-mean (denoted by an overbar) background vertical DSE gradient, expressed as

$$\omega' = \frac{Q_1'}{\frac{\partial \bar{s}}{\partial p}}. \tag{3}$$

Equation (3) highlights the competing effects of anomalous diabatic heating and mean static stability on determining the MJO circulation anomaly (Bui and Maloney 2018; Cui and Li 2019).

3. Basic MJO features in two twentieth-century datasets

To verify the quality of the two twentieth-century reanalysis datasets in revealing the characteristics of the MJO, we compared the basic MJO features in 20CR and ERA-20C with

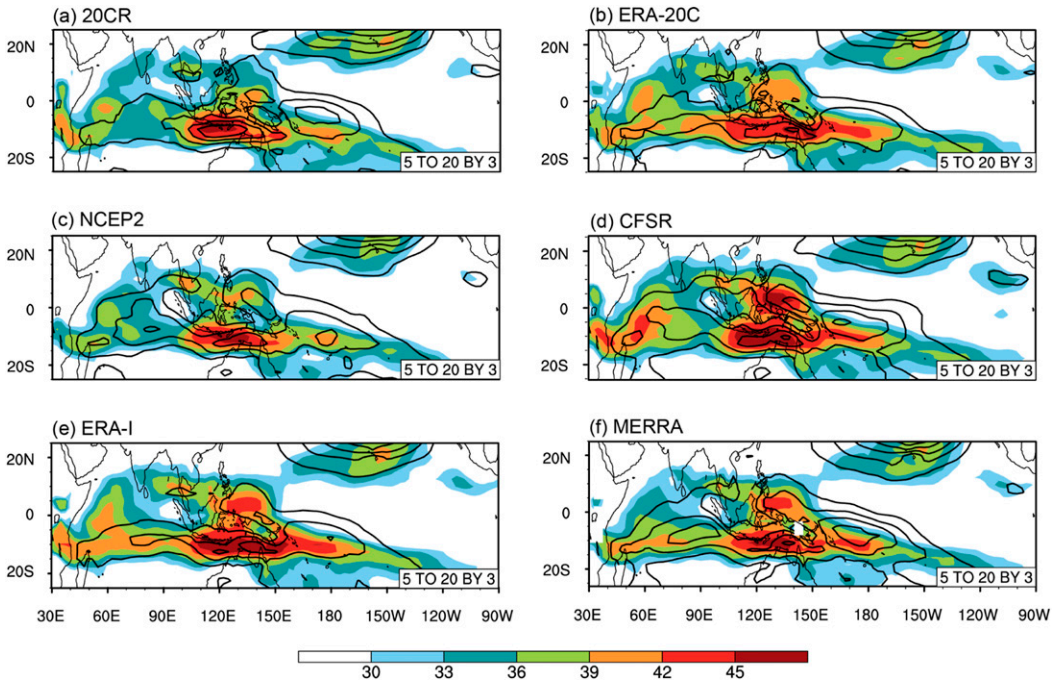

FIG. 1. Variances of 20–90-day filtered 850-hPa zonal wind (contour; $m^2 s^{-2}$) during boreal winters (November–April) of 1979–2009 and the ratios to their corresponding total (unfiltered) variances (shading; %) derived from (a) 20CR, (b) ERA-20C, (c) NCEP-2, (d) CFSR, (e) ERA-Interim, and (f) MERRA.

other reanalysis datasets (NCEP-2, CFSR, ERA-Interim, and MERRA) during the boreal winter (November–April) of 1979–2009. The amplitude and geographical distribution of MJO-related U850 variability were evaluated (Fig. 1). Both 20CR (Fig. 1a) and ERA-20C (Fig. 1b) captured the maximum MJO variance region over the Indo-Pacific warm pool (Zhang 2005), with comparable amplitude of the other reanalysis datasets. The pattern correlation coefficients of MJO circulation variance in the two twentieth-century reanalysis datasets against the other reanalysis datasets are high (>0.93) (Table 1). The quantitative differences between the two twentieth-century datasets and other reanalysis datasets, as represented by the normalized root-mean-square error (RMSE), are small (0.23–0.43).

Spectral analysis also suggested that the twentieth-century reanalysis datasets captured the equatorial MJO signals well during the boreal winter (Fig. 2). Both datasets (Figs. 2a and 2b) clearly contain the eastward propagation signals with a period of 20–90 days and a planetary scale of zonal wavenumber 1, consistent with the other reanalysis datasets (Figs. 2c–f). The high pattern correlation coefficients and low RMSEs for the spectra in Table 1 confirm the capability of 20CR and ERA-20C in capturing the MJO's spectral features. We further applied MEOF analysis using NOAA OLR and wind fields (U850 and U200) in the individual reanalysis datasets to examine the spatial structures of leading modes associated with the MJO (Fig. 3), as proposed by Wheeler and Hendon (2004) and Waliser et al. (2009). The first baroclinic mode of MJO circulation, with a low-level easterly (westerly) and a high-level westerly (easterly) to the east (west) of MJO convection, can be clearly identified in 20CR (Fig. 3a) and ERA-20C (Fig. 3b), in agreement with observations (Madden and Julian 1971, 1972; Wheeler and Hendon 2004). The first two leading modes accounted for ~34% of the total variance from the two twentieth-century datasets (Figs. 3a,b), similar to the results from the other datasets (Figs. 3c–f), albeit slightly smaller in amplitude.

These results indicate that, although only the observed surface signals were assimilated, the two twentieth-century reanalysis systems are capable and reliable in capturing the MJO's characteristics (Gao et al. 2016; Cui et al. 2019). Note that the aim of this study is not to assess the reanalysis datasets, but to search for reliable features of MJO variation during the entire twentieth century. Thus, the robustness of the two datasets and their consistency with the other datasets remain the base for the following analyses.

4. Changes in MJO amplitude over the twentieth century

To compare the temporal evolutions of MJO intensity $[(PC1^2+PC2^2)^{1/2}]$ over the twentieth century in different datasets, we obtained the PCs by projecting the 20–90-day U200, U850, and OLR from each reanalysis dataset onto the first two MEOF modes defined by Wheeler and Hendon (2004) and then calculated the MJO intensity in each decade from 1900 to 2010 (Fig. 4). Following Wheeler and Hendon (2004), the MEOF modes of MJO were derived using the 20–90-day wind fields from the NCEP-1 and OLR from NOAA over the period of 1979–2010. The two twentieth-century reanalysis datasets

TABLE 1. Pattern correlation coefficients for variance maps (Fig. 1) of 20–90-day U850 and the wavenumber–frequency (W-F) spectra (Fig. 2) in two twentieth-century reanalysis datasets against other reanalysis datasets. The normalized root-mean-square errors are shown in the lower half of the table.

		NCEP-2	CFSR	ERA-Interim	MERRA
		Pattern correlation			
20CR	Variance map	0.93	0.95	0.95	0.93
	W-F spectra	0.98	0.98	0.97	0.98
ERA-20C	Variance map	0.97	0.95	0.98	0.96
	W-F spectra	0.99	0.99	0.99	0.99
		Normalized RMSE			
20CR	Variance map	0.38	0.35	0.33	0.43
	W-F spectra	0.23	0.30	0.27	0.30
ERA-20C	Variance map	0.32	0.37	0.23	0.37
	W-F spectra	0.16	0.39	0.14	0.34

show consistent changes in MJO amplitude after the 1920s (Fig. 4). Both datasets reveal pronounced decadal variation with an increasing trend. A remarkable strengthening of the MJO was detected from the 1930s to the 1960s, which leveled off slightly afterward. The decadal variation of MJO amplitude (with a significant increase before the 1970s) is also seen in the NCEP-1 (Fig. 4). The increase in MJO amplitude during the 1930s to the 1960s is also seen in the Oliver–Thompson index (I^{HR}). However, the slope of the increasing trend in I^{HR} is smaller than that in the other datasets (Fig. 4). The incompatible

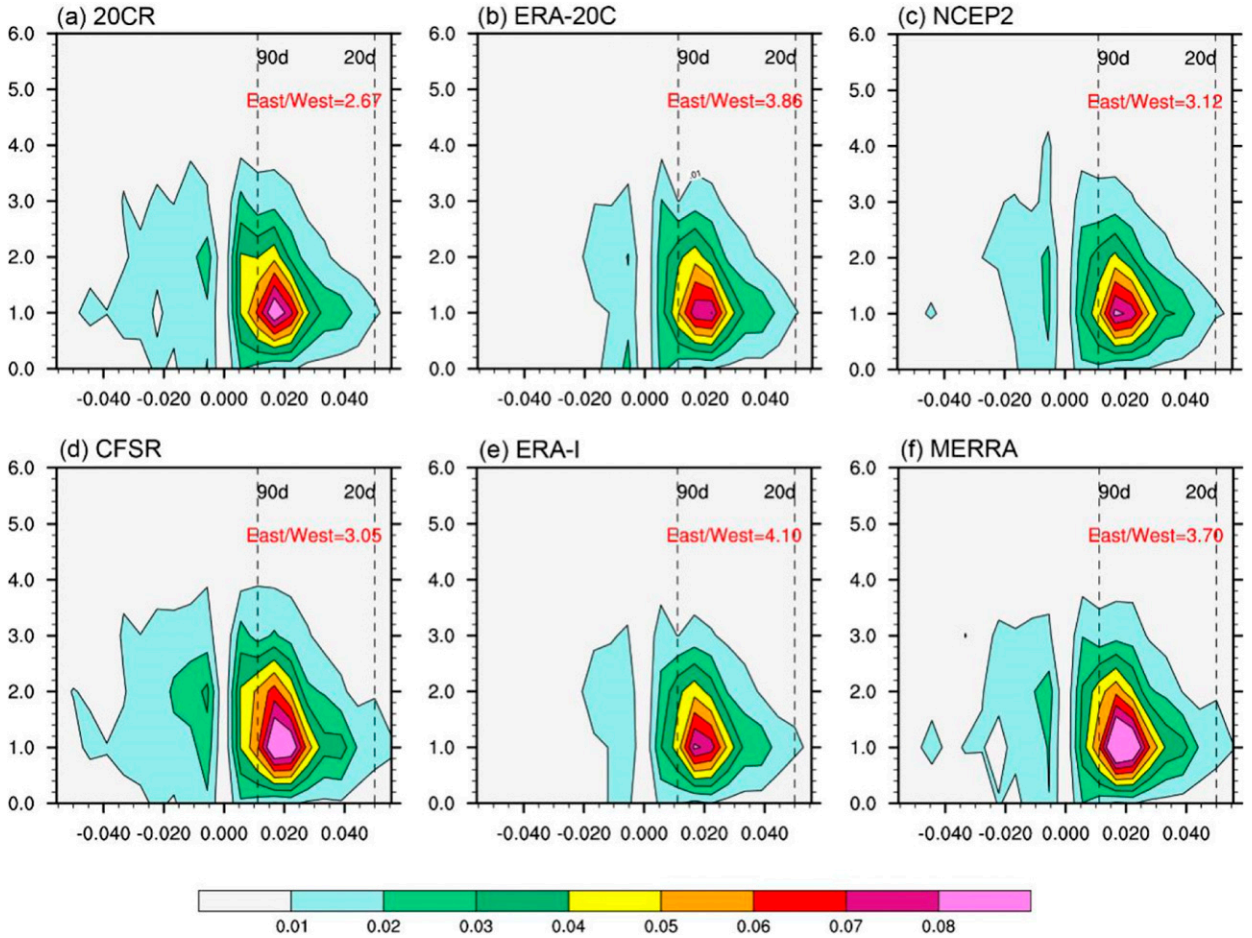

FIG. 2. As in Fig. 1, but for the wavenumber–frequency spectra of equatorial (10°S–10°N) averaged 850-hPa zonal wind (shading; $m^2 s^{-2}$). The east-to-west power ratios of 20–90-day components are highlighted in red. Only the climatological seasonal cycle and time mean for each November–April segment were removed before calculating the spectra.

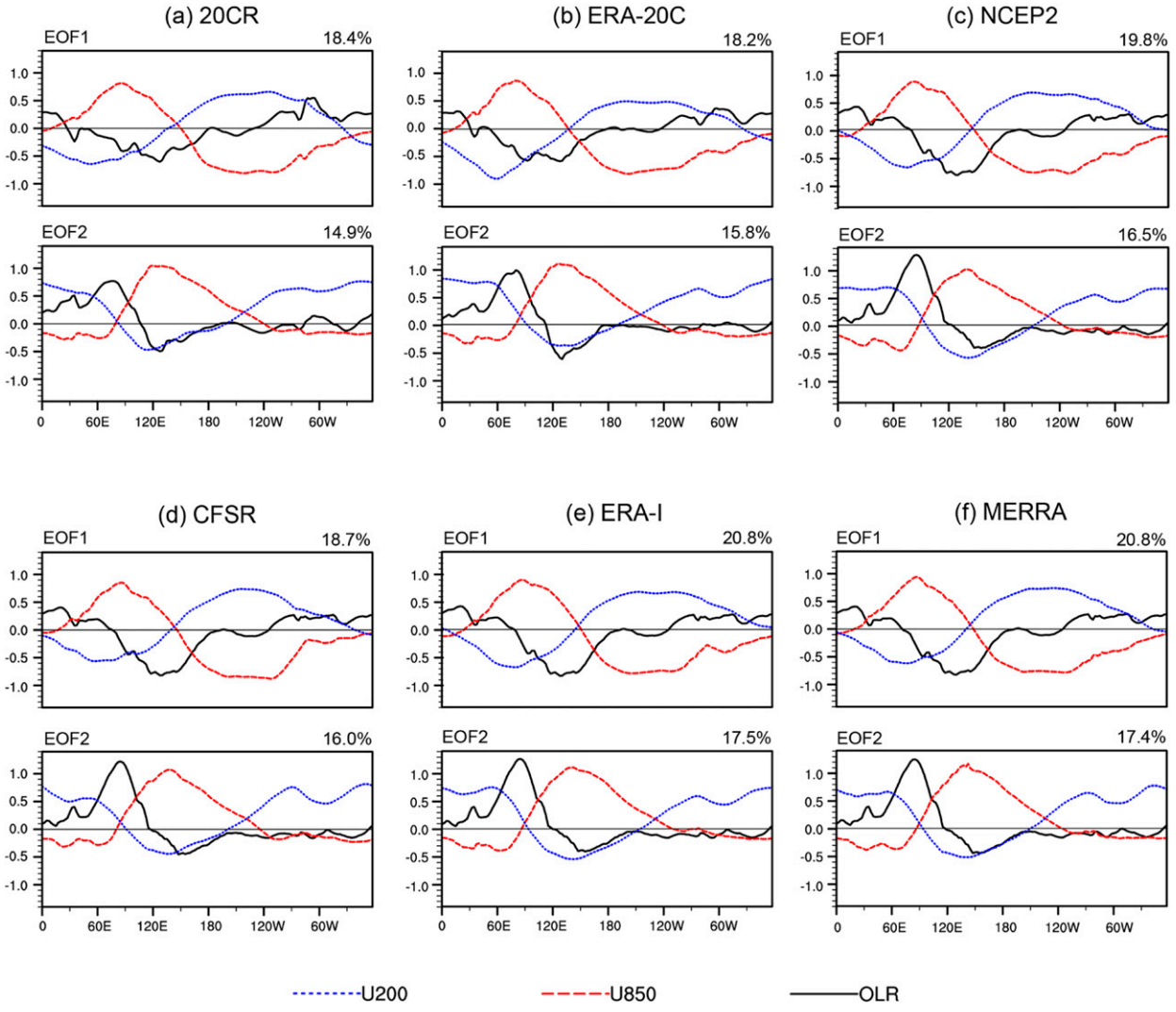

FIG. 3. As in Fig. 1, but for the first two MEOF modes of equatorial (15°S–15°N) averaged 20–90-day U850 (red), U200 (blue), and OLR (black). The explained variance of each mode is shown at the upper right of each panel.

trends shown by I^{HR} and the two twentieth-century reanalysis datasets might be attributable to the different methods used to extract the MJO signals in our study. Similar to the RMM index of Wheeler and Hendon (2004), the MJO signals derived from the MEOF analysis for the reanalysis datasets were based on global-scale OLR and circulation anomalies at the equator. In contrast, I^{HR} was defined by using only 12 locations (Fig. 5a), where the surface pressure data have better quality (i.e., with smaller intermember standard deviations among the 56 ensemble members of 20CR) and show a stronger relationship with the MJO index of Wheeler and Hendon (2004) (Oliver and Thompson 2012).

To reduce the uncertainty due to data quality, we calculated the variances of MJO-related fields in each winter at the 12 sites suggested by Oliver and Thompson (2012), and then averaged the 12 values to present the MJO amplitude. The resultant fluctuations of MJO amplitude at the decadal time scale over the twentieth century are shown in Fig. 5b. The increasing tendencies in MJO convection (OLR) and circulation (U850) amplitude can still be observed (Fig. 5b), while their slopes are weakened compared to those detected in Fig. 4. Similar to the results of I^{HR}, the MJO-related surface pressure revealed a nonsignificant trend but clear multidecadal variation (Figs. 4 and 5b). Note that, regardless of the method (Wheeler and Hendon 2004; Oliver and Thompson 2012) and variables used to estimate the MJO signals and their amplitude (Figs. 4 and 5), the boreal winter MJO tended to weaken during the earlier decades of the study period (i.e., 1920–49, referred to herein as D1), but strengthen during the later decades of 1970–99 (D2). To confirm the choice of D1 and D2 is reasonable, we plotted the time series of MJO amplitude index from 20CR, ERA-20C, and NCEP-1 (not shown), and found that D1 and D2 did reveal the contrast in MJO intensity in all three datasets. Moreover, we compared the differences in MJO intensity of the 30-yr

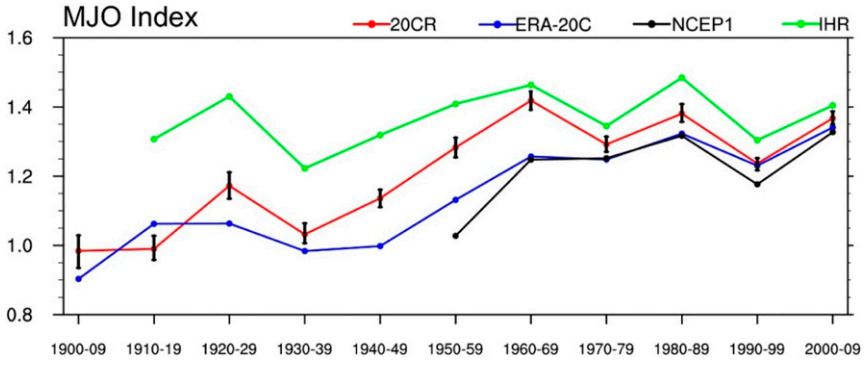

FIG. 4. Temporal evolutions of MJO amplitude $[(PC1^2+PC2^2)^{1/2}]$ in each decade from the beginning of the twentieth century to the first decade of the twenty-first century. Red, blue, and black lines denote the MJO amplitude derived from 20CR, ERA-20C, and NCEP-1, respectively. The vertical bars represent the range of MJO amplitude based on Monte Carlo experiments (repeated 1000 times) for the 56 members of 20CR. Green line denotes the historical reconstruction of the MJO index (I^{HR}) proposed by Oliver and Thompson (2012).

climate mean states in the first half century (1920–49, 1930–59, and 1940–69) and the second half century (1950–79, 1960–89, and 1970–99) derived from the two twentieth-century reanalysis datasets. The differences in MJO amplitude between 1920–49 and 1970–99 are large and statistically significant. These results suggest the feasibility and reliability of our definitions for D1 and D2.

By comparing the wavenumber–frequency spectra between D1 and D2 (not shown), we noticed that the centers of spectral power maximized at the same bands of frequency and

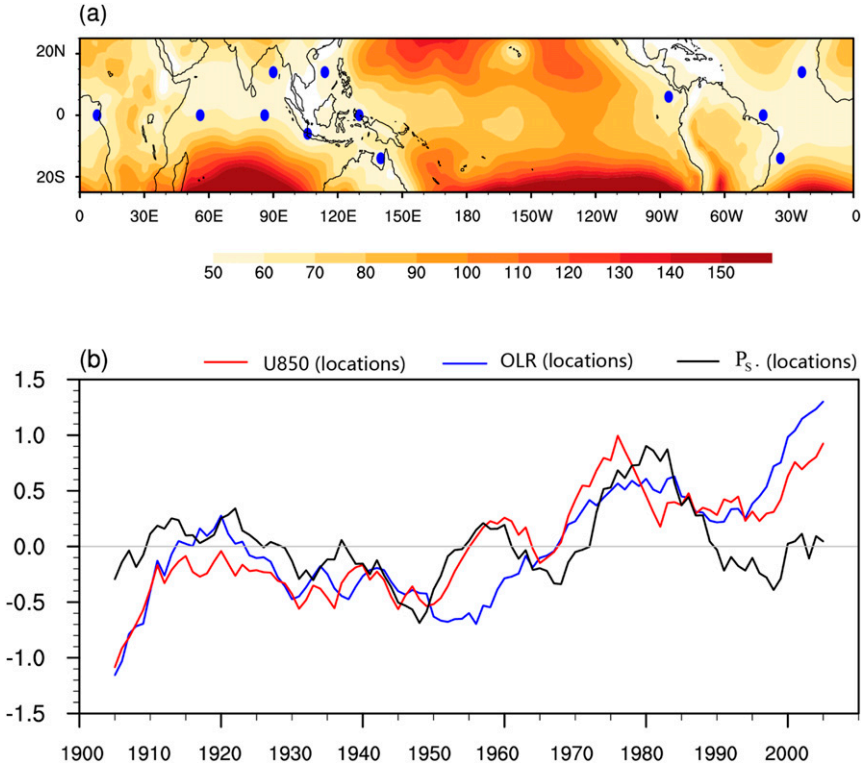

FIG. 5. (a) Standard deviations of 1900–2010 surface pressure (Pa) among 56 members of 20CR. Blue dots mark the chosen locations for data reconstruction in Oliver and Thompson (2012). (b) Temporal evolutions of 11-yr-running-averaged variance of 20–90-day filtered U850 (red), OLR (blue), and surface pressure (black) based on the 12 sites in (a). The variances in (b) were normalized by a unit standard deviation.

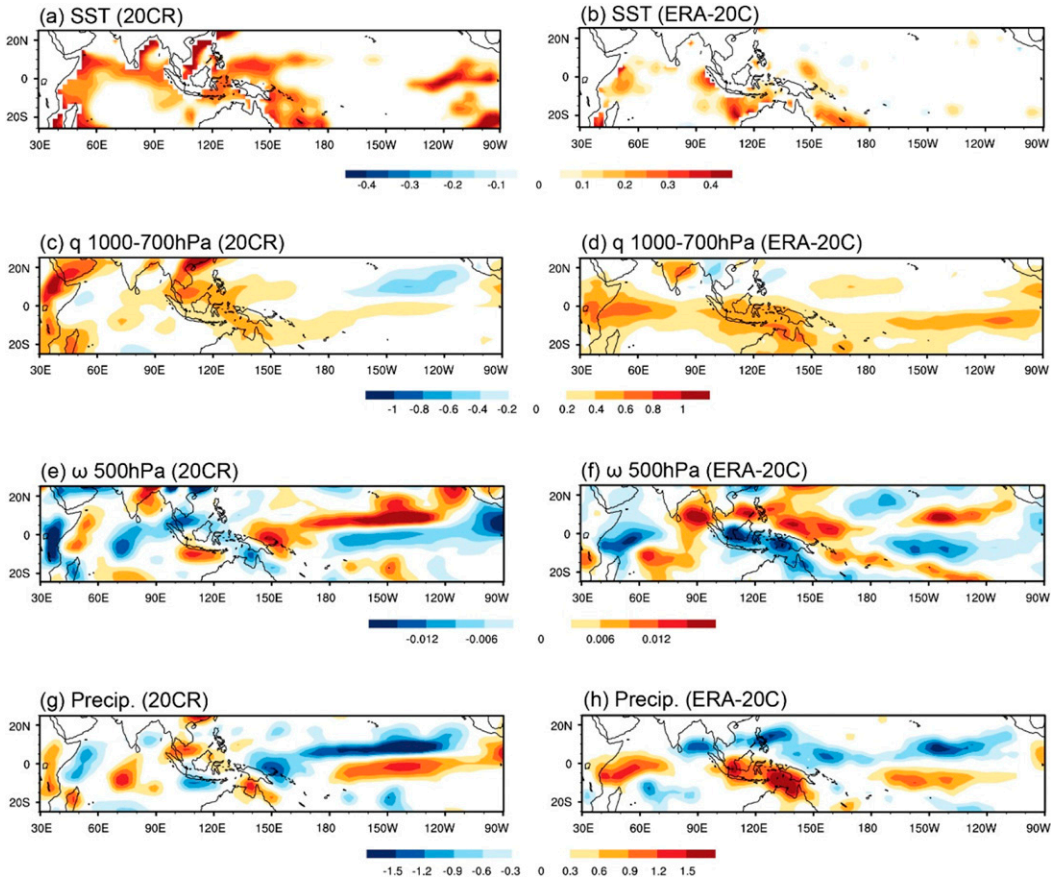

FIG. 6. Changes in the seasonal mean states of (a),(b) prescribed SST (K), (c),(d) 1000–700-hPa averaged moisture (g kg^{-1}), (e),(f) 500-hPa vertical velocity (Pa s^{-1}), and (g),(h) precipitation (mm day^{-1}) between the two periods investigated (D2 minus D1). The results of (left) 20CR and (right) ERA-20C. Only the regions with a statistically significant change at the 90% confidence level are shown.

wavenumber. This suggests that no obvious changes were detected for the MJO spatial structure and phase speed. As for the propagation features, we found that the east-to-west power ratios of precipitation and 850-hPa zonal wind were similar in 20CR during D1 and D2, while they increased in the recent decade in ERA-20C. The enhanced eastward-propagating MJO was reported in previous modeling studies (Adames et al. 2017; Cui and Li 2019). From both datasets, the pronounced changes in power spectra consistently appeared in the 20–90-day band (i.e., MJO amplitude), in agreement with the results of Figs. 4 and 5. Thus, we will focus on addressing the factors that regulate the changes in MJO amplitude at the multidecadal time scale.

Considering that the MJO perturbations are strongly modulated by background thermodynamic and dynamic conditions, we first examined large-scale mean state changes from D1 to D2 (Fig. 6). Along with the global warming over the twentieth century, the wintertime SST showed significant increases over the tropical Indian Ocean and western Pacific warm-pool regions in D2 (Figs. 6a,b). These changes could be related to the regime shift of global-scale SST pattern in the 1970s (Baines and Folland 2007). Because the amplitude and warming patterns of prescribed SST fields for the two reanalysis datasets revealed some differences, detailed distributions of multidecadal changes in moisture and vertical motion anomalies in 20CR (Figs. 6c,e) and ERA-20C (Figs. 6d,f) were slightly different. In general, positive moisture anomalies in the lower troposphere appeared over the warmer SST regions of the Indo-Pacific warm pool in both datasets (Figs. 6c,d). Unlike the thermodynamic effects with a spatially uniform change over the Indo-Pacific warm pool, the changes in atmospheric circulation showed regional features. Large-scale anomalous ascending motions were observed over the Maritime Continent, while anomalous descending motions prevailed over the western Pacific (Figs. 6e,f). The upward motion and increased moisture content over the Maritime Continent led to enhanced precipitation there (Figs. 6g,h).

To identify the spatial distribution of MJO amplitude change, we compare the life cycle evolutions of equatorial MJO precipitation and U850 during the two decadal periods (Fig. 7). In both D1 and D2, the eastward propagation of MJO precipitation anomalies from the equatorial Indian Ocean to the western and central Pacific is well illustrated by the phase–longitude diagram using 20CR and ERA-20C (Figs. 7a,b,d,e).

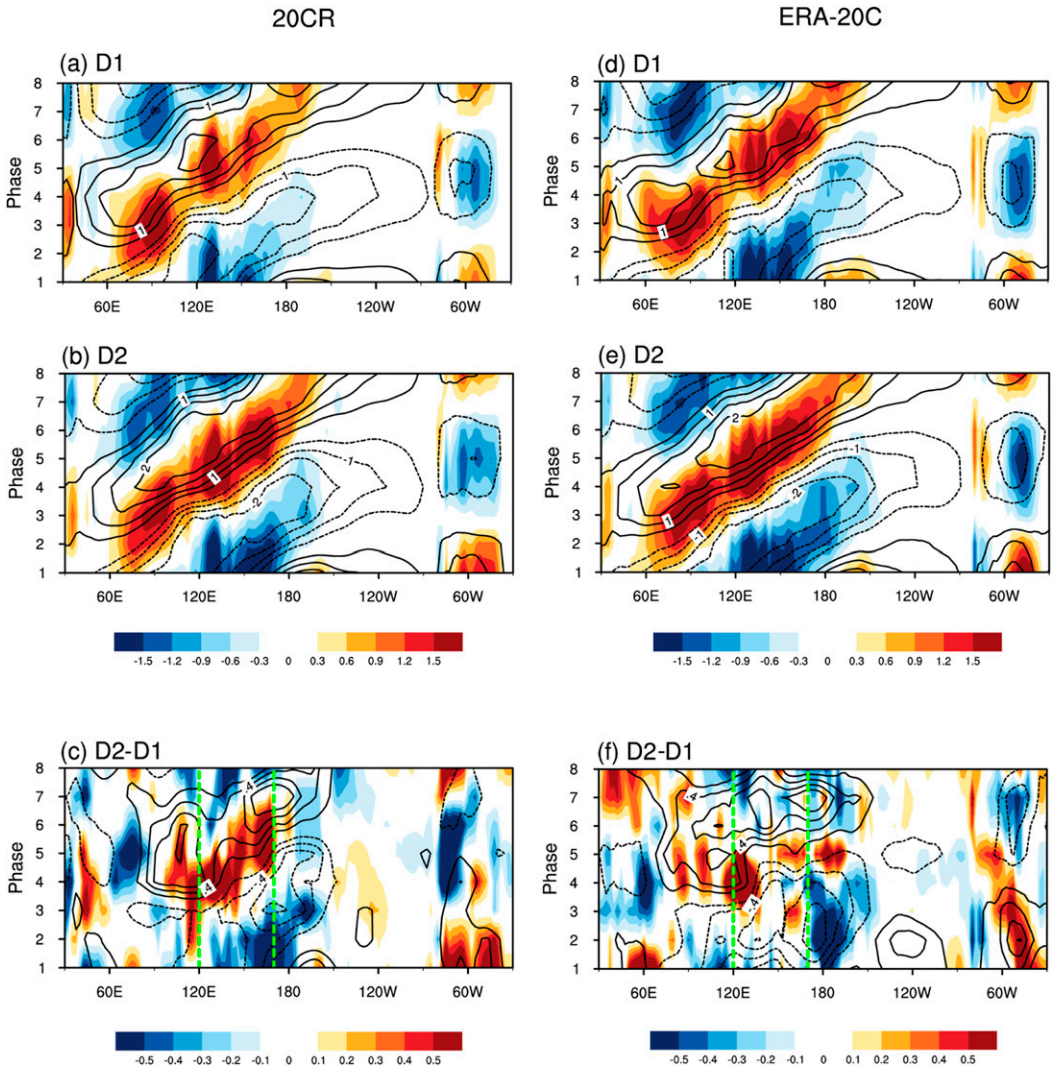

FIG. 7. Phase–longitude evolutions of 20–90-day precipitation (shading; mm day^{-1}) and U850 (contour; m s^{-1}) anomalies averaged over 15°S–0° during boreal winter in (a) D1 and (b) D2, and (c) their differences (D2 minus D1) derived from 20CR. Only the changes with statistical significance at the 90% confidence level are shown in (c). (d)–(f) As in (a)–(c), but for ERA-20C.

To the east (west) of the MJO precipitation, the low-level easterly (westerly) anomalies associated with Kelvin (Rossby) waves also propagated eastward with the MJO convection. Again, the two twentieth-century reanalysis datasets realistically capture the coupled structures of convection and circulation. It is clear that the MJO had larger amplitude in D2 than in D1 (Figs. 7a,b,d,e). The most significant increases in MJO precipitation and U850 occurred over the western Pacific region (120°–170°E), revealed by both 20CR (Fig. 7c) and ERA-20C (Fig. 7f). Therefore, we selected the western tropical Pacific (120°–170°E, 15°S–0°) as the key region for moisture budget diagnosis to understand the major processes responsible for the strengthened MJO precipitation in D2.

Figure 8 shows the temporal evolutions of MJO-related precipitation anomalies over the key region composited by all cases with area-averaged 20–90-day precipitation greater than one standard deviation. Day 0 is defined as the time when the precipitation anomaly reached its maximum for each enhanced MJO precipitation case (Fig. 8a). Compared to D1, the MJO precipitation in D2 had larger amplitude (Fig. 8b), consistent with the results of Fig. 7. The increase in MJO precipitation amplitude in 20CR was larger than that in ERA-20C.

The supply of moisture is important in supporting the growth of MJO precipitation (Benedict and Randall 2007; Hsu and Li 2012; Sobel and Maloney 2013). We also examined evolutions of moisture anomalies in the column associated with the multidecadal changes in MJO precipitation. As shown in Fig. 9, both 20CR and ERA-20C revealed abundant moisture in the lower to middle troposphere as the enhanced MJO precipitation occurred from days −5 to +5 (Figs. 9a,e). The

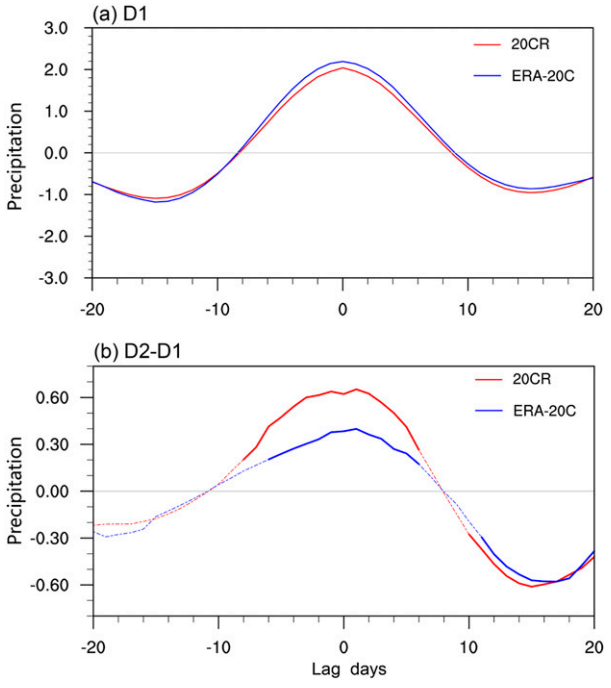

FIG. 8. (a) Evolution of 20–90-day precipitation (mm day^{-1}) over the key region in the western Pacific warm pool (120°–170°E, 15°S–0°) during D1, and (b) its changes (D2 minus D1). Day 0 represents the date when the area-averaged precipitation anomaly reached its maximum for each active MJO convective event (i.e., amplitude greater than one standard deviation). Red and blue curves denote the results derived from 20CR and ERA-20C, respectively. Solid segments in (b) denote the changes are statistically significant at the 95% confidence level, and the dashed ones indicate insignificant changes.

increased precipitation anomalies in D2 was linked to increased column moisture. The most significant increase in moisture in D2 relative to D1 appeared at the boundary layer and in the midtroposphere (Figs. 9a,e). The convergence of moisture flux anomalies also increased noticeably in the lower to middle troposphere (1000–500 hPa) during D2 in both datasets (Figs. 9b,f), which contributed to the increases in moisture and precipitation. Horizontal moisture convergence $[-(q\nabla \cdot V)']$ contributed predominantly to moisture flux convergence (Figs. 9c,g); however, horizontal moisture advection $[-(V \cdot \nabla q)']$ showed a negligible effect (with small negative values) on the enhanced precipitation from days −5 to +5 (Figs. 9d,h). It is worth noting that the enhancements in moisture, moisture flux, and horizontal moisture convergence were of larger amplitude in 20CR than in ERA-20C, in agreement with a larger increase in the MJO precipitation anomaly over the western Pacific warm pool in 20CR compared to ERA-20C (Figs. 7 and 8). The results are similar to previous findings that the low-level moisture convergence near the MJO convective center results in upward moisture transport and thus favors the precipitation anomaly (Hendon and Liebmann 1994). This is also the key process responsible for the enhanced MJO convection under global warming (Zelinka and Hartmann 2011; Singh and O'Gorman 2012; Chang et al. 2015).

A number of studies (e.g., Hsu and Li 2012; Chang et al. 2015) indicated that the anomalous convergence of seasonal-mean moisture $[-(\overline{q}\nabla \cdot V')]$ is the leading process causing the enhanced moisture convergence anomaly that supports the MJO-related convection and precipitation anomalies. To further examine the relative contributions of mean moisture change and anomalous circulation change to the multidecadal change in moisture convergence anomaly (and thus MJO precipitation), we decomposed the changes in $-(\overline{q}\nabla \cdot V')$ as follows:

$$\Delta(\overline{q}\delta') = \overline{q}_1\Delta\delta' + \Delta\overline{q}\delta'_1 + \Delta\overline{q}\Delta\delta', \quad (4)$$

where Δ denotes the change in D2 relative to D1 (D2 minus D1), and the subscripts 1 and 2 represent the state in D1 and D2, respectively. For simplicity, δ' represents horizontal convergence anomaly $[-(\nabla \cdot V)']$. Thus, the decadal change (D2 minus D1) in anomalous convergence of mean moisture $\Delta(\overline{q}\delta')$ may come from the decadal change in MJO-related convergence $\overline{q}_1\Delta\delta'$, even if the winter-mean moisture fields do not change, and from the decadal change in the mean moisture $\Delta\overline{q}\delta'_1$, as well as both changes in anomalous circulation and mean moisture $\Delta\overline{q}\Delta\delta'$.

The diagnostic results of Eq. (4) are shown in Fig. 10. Compared to D1, the MJO-related convergence of mean moisture during D2 was enhanced from day −10 to +5 (before and at the occurrence of MJO precipitation) in the lower to middle troposphere. These changes were observed in both 20CR (Fig. 10a) and ERA-20C (Fig. 10e). This change largely came from $\overline{q}_1\Delta\delta'$, that is, the contribution of multidecadal change in MJO-related convergence $\Delta\delta'$ instead of the mean moisture change (Figs. 10b,f). In contrast, the contribution of mean moisture change at the multidecadal time scale ($\Delta\overline{q}\delta'_1$) was much smaller (about one order of magnitude smaller) than that of the effect of anomalous circulation change (Figs. 10b,c,f,g). The nonlinear processes associated with both anomalous circulation change and mean moisture change ($\Delta\overline{q}\Delta\delta'$) were also of small amplitude (Figs. 10d,h). The key process accounting for the enhanced MJO precipitation over the twentieth century found here ($\overline{q}_1\Delta\delta'$) is different from that for the MJO precipitation intensification under future warming scenarios. For the future scenarios, changes in mean moisture $\Delta\overline{q}\delta'_1$ play a leading role in strengthening the MJO variability of precipitation (e.g., Chang et al. 2015; Wolding et al. 2017; Bui and Maloney 2018; Maloney et al. 2019). This difference may be attributable to the increasing rates of SST and moisture, which were relatively weak in the twentieth century (not shown).

5. Factors regulating the amplitude changes in circulation anomaly

The enhancement of the MJO circulation anomaly shown in the moisture diagnosis can be confirmed by comparing the anomalous vertical motion associated with the MJO during the two decadal periods (Fig. 11). Both 20CR and ERA-20C showed significantly enhanced ascending motion anomalies in the midtroposphere during the MJO precipitation period

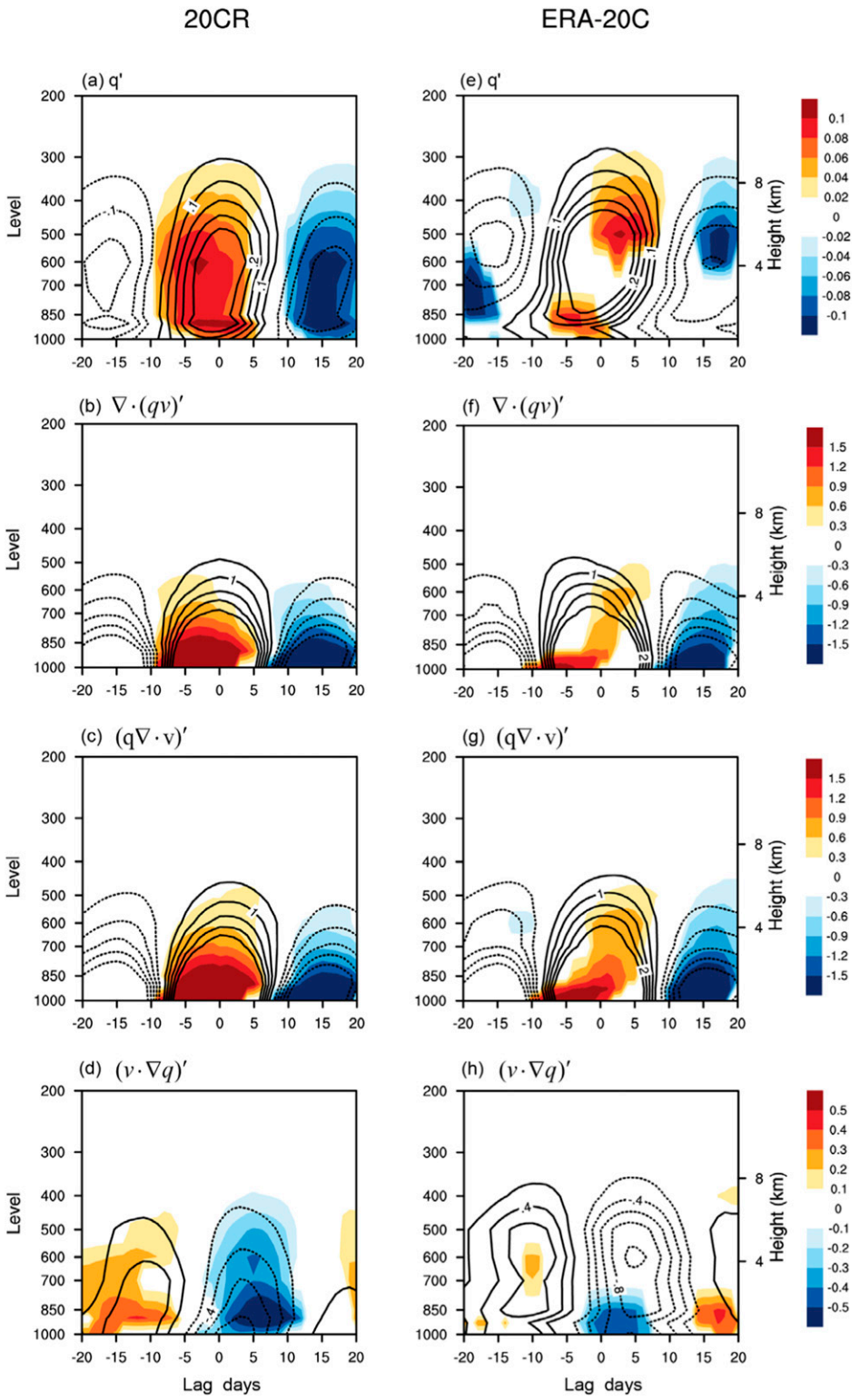

FIG. 9. As in Fig. 8, but for the vertical structures of 20–90-day (a) moisture anomalies ($g\,kg^{-1}$), (b) moisture flux ($10^{-6}\,g\,kg^{-1}\,s^{-1}$), (c) moisture convergence ($10^{-6}\,g\,kg^{-1}\,s^{-1}$), and (d) moisture advection ($10^{-6}\,g\,kg^{-1}\,s^{-1}$) derived from 20CR. Contours indicate the results in D1, while shading presents the changes (D2 minus D1). Only the changes with statistical significance at the 90% confidence level are shown. (e)–(h) As in (a)–(d), but for ERA-20C.

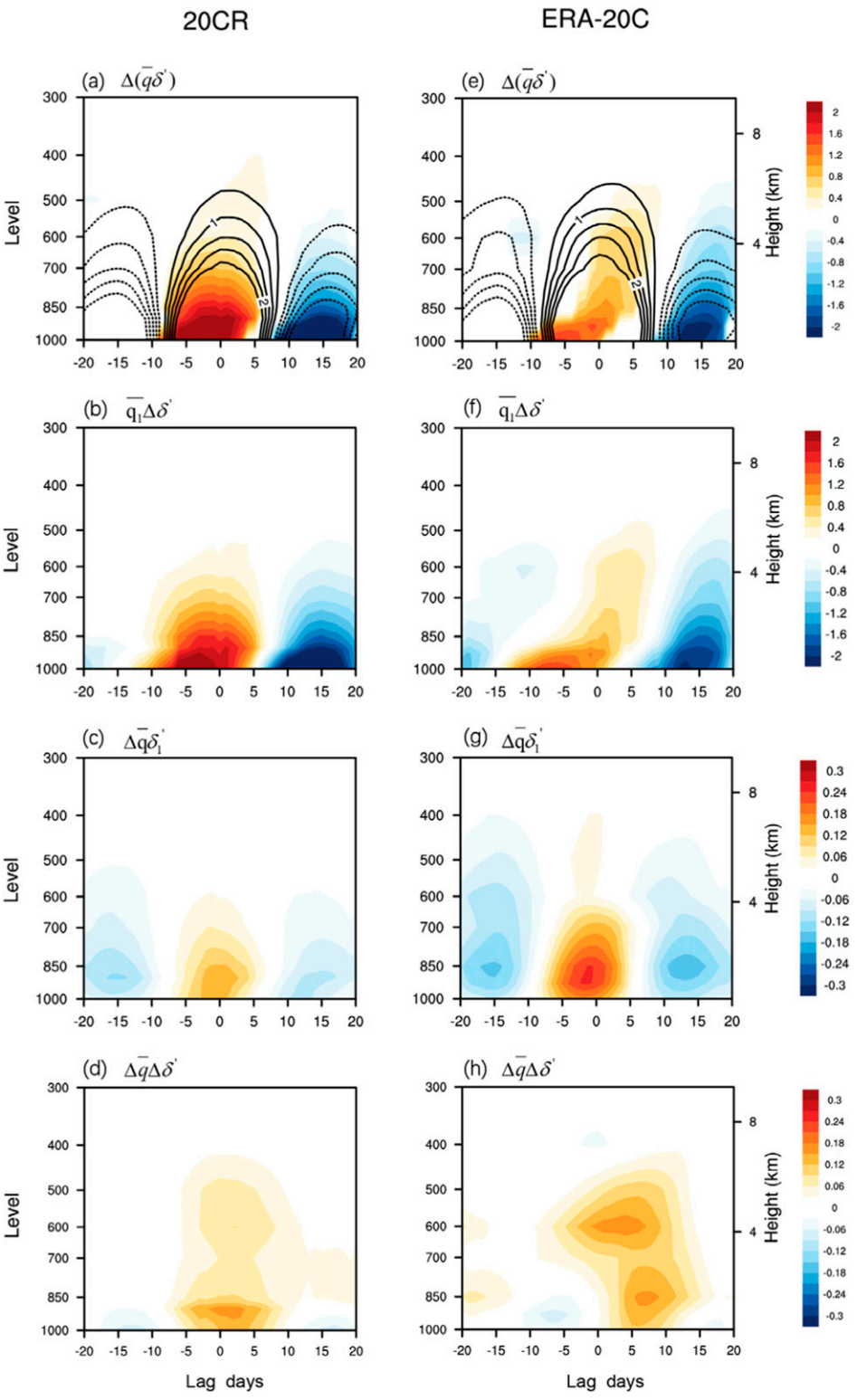

FIG. 10. As in Fig. 9, but for relative contributions of moisture convergence anomaly from different time scale components to the decadal change in $-(\overline{q}\nabla\cdot V')$, based on the diagnosis of Eq. (4). (a) MJO convergence of the mean moisture $-(\overline{q}\nabla\cdot V')$ in D1 (contours) and its decadal change (D2 minus D1) $\Delta(\overline{q}\delta')$, and the contributions by (b) anomalous circulation change $\overline{q}_1\Delta\delta'$ and (c) mean moisture change $\Delta\overline{q}\delta_1'$, and (d) both changes $\Delta\overline{q}\Delta\delta'$. Units are $10^{-6}\,\mathrm{g\,kg^{-1}\,s^{-1}}$.

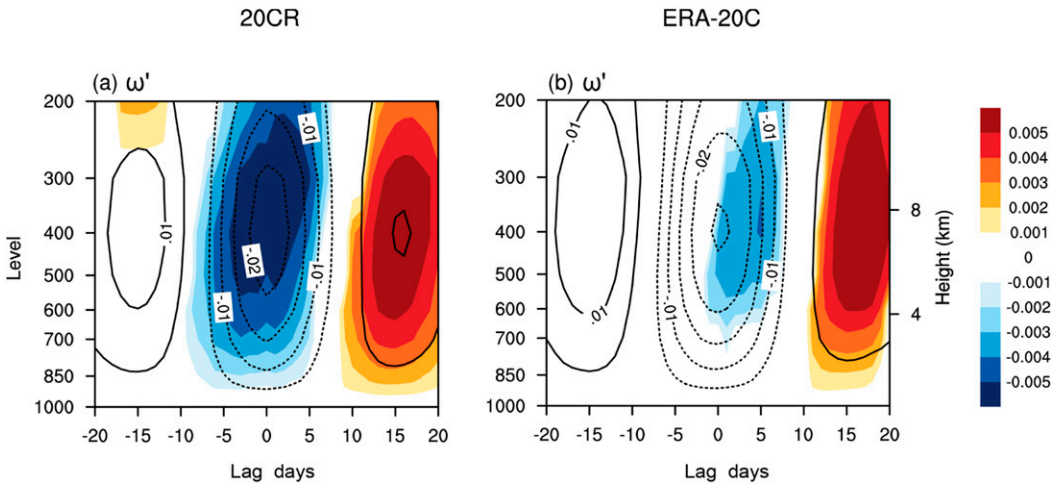

FIG. 11. As in Figs. 9a and 9e, but for 20–90-day vertical velocity (Pa s^{-1}).

(from days −5 to +5). In 20CR, the MJO vertical velocity anomaly increased by 29.3% during D2 with respect to D1 (Fig. 11a), which was larger than that (12.4%) detected in ERA-20C (Fig. 11b). The enhanced ascending motion anomaly was associated with stronger moisture convergence and thus moisture vertical advection (not shown), favoring a larger MJO precipitation anomaly in D2 (Figs. 8–10). The larger enhancement of MJO circulation in 20CR (Fig. 11) can also explain the larger increase in MJO precipitation compared to the results of ERA-20C (Fig. 8b).

The next question that needs to be addressed is the cause of the enhanced MJO circulation in D2. According to Eq. (3), MJO-related vertical velocity ω' is positively correlated with anomalous diabatic heating Q_1', but inversely correlated with mean vertical DSE gradient $\partial\overline{s}/\partial p$. Thus, the fractional change in the anomalous vertical velocity between the two decadal periods (D2 minus D1) can scale with the difference between the anomalous diabatic heating change and vertical DSE gradient change,

$$\Delta\omega' = \Delta\left(\frac{Q_1'}{\frac{\partial\overline{s}}{\partial p}}\right) = \Delta Q_1' - \Delta\left(\frac{\partial\overline{s}}{\partial p}\right). \tag{5}$$

As shown in Fig. 12a, the change in ω' can be described by the change in the ratio of Q_1' to $\partial\overline{s}/\partial p$ for both datasets, suggesting that the budget analysis of Eq. (5) is reliable. The anomalous heating tended to enhance and was partly offset by enhanced mean static stability in D2. The increased static stability under the warming climate in the twentieth century was induced by significant upper-tropospheric warming (not shown) and acted to weaken the anomalous circulation, similar to the features under future warming scenarios (Bui and Maloney 2018). Different from the future projection results, the enhancement of anomalous heating overwhelmed the effect of increased static stability. Thus, the MJO-related circulation showed enhanced amplitude. The larger increases in the vertical motion anomaly (Fig. 11) and moisture convergence (Fig. 10) in 20CR than in ERA-20C can be linked to the smaller negative effect of increased static stability (Fig. 12b).

The diabatic heating anomaly mainly consists of latent heating anomaly and radiative heating anomaly, both of which are crucial for MJO development (Lin and Mapes 2004; Jiang et al. 2011; Ling et al. 2013). Figure 13 compares the contributions of latent heating, represented by the apparent moisture sink (Q_2 in Yanai et al. 1973), and radiative heating related to longwave and shortwave processes, respectively. The latent heating anomaly played the dominant role in inducing the enhanced circulation anomaly in D2 in both 20CR and ERA-20C (Fig. 13). The enhanced latent heating anomaly was produced by an increased precipitation anomaly, which further strengthened the circulation and precipitation, indicating the convection–circulation positive feedback of the MJO under global warming (Cui and Li 2019). Radiative heating also contributed to the enhanced circulation anomaly in D2 (Fig. 13). As the climate became warmer in D2, the MJO-related moisture and precipitation anomalies would have enhanced the longwave radiative heating (Wolding et al. 2017). The influence of shortwave radiative heating on the circulation anomaly at the multidecadal time scale seemed to be weak (Fig. 13). Previous studies have highlighted the importance of longwave radiation to MJO dynamics (Lin and Mapes 2004; Jiang et al. 2011). In this study, we found that the multidecadal changes in both latent and longwave radiative heating anomalies contributed to the change in MJO precipitation amplitude by inducing vertical motion anomaly. Further comparison of MJO heating profiles revealed that the centers of anomalous diabatic heating did not change from D1 to D2 in 20CR, while they lifted slightly during D2 in ERA-20C (not shown). The more top-heavy structure of warming (Bui and Maloney 2019b) was found in ERA-20C. This change of heating profile in ERA-20C might have caused the smaller increase in ascending motion anomaly and less efficiency of vertical moisture advection (Bui and Maloney 2018) compared to those in 20CR. Thus, the enhancement of MJO precipitation in ERA-20C was of smaller amplitude than that in 20CR (Fig. 8b).

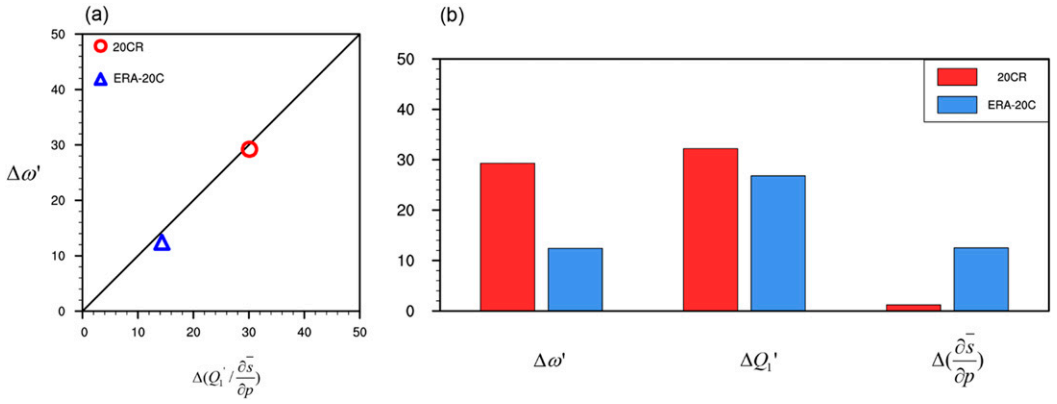

FIG. 12. (a) Percentage changes (i.e., normalized decadal changes in a variable by its value in the earlier decade; %) of MJO-related vertical velocity (y axis) vs the ratio of MJO apparent heating to the dry static energy (DSE) gradient (x axis) derived from 20CR (red circle) and ERA-20C (blue triangle). (b) Comparison of percentage changes (%) in MJO-related (shown from left to right) vertical velocity, diabatic heating, and vertical gradient of mean DSE between 20CR (red) and ERA-20C (blue). These were calculated during the MJO active period (from days −5 to +5) and averaged from 600 to 300 hPa.

6. Summary

Based on two century-long reanalysis datasets (20CR and ERA-20C), which are both adequate in describing the amplitude, spatial pattern, and propagating features of MJO-related variability (Cui and Li 2019), we examined the changes in MJO precipitation and the mechanisms responsible for these changes over the twentieth century. To increase the reliability and robustness of MJO variation signals during the entire twentieth century, various definitions of MJO precipitation and circulation amplitude, as well as datasets, were used. Significant multidecadal variations of MJO amplitude along with an increasing trend were detected in 20CR, ERA-20C, NCEP-1, and the Oliver–Thompson MJO index. Various MJO amplitude indices using different data consistently showed enhanced MJO precipitation and circulation amplitude during the later decadal period of 1970–99 (D2) with respect to those during the earlier decadal period of 1920–49 (D1).

The most evident increases in MJO precipitation amplitude in D2 relative to D1 occurred over the western Pacific warm-pool region (120°–170°E, 15°S–0°), where the winter-mean SST and moisture in D2 were significantly higher than those in D1. To understand the processes inducing the enhanced MJO precipitation intensity, the MJO-related moisture budget equation was diagnosed. An increased moisture anomaly induced by horizontal moisture convergence anomaly was consistently observed over a key region with enhanced MJO precipitation amplitude, indicating that the horizontal moisture convergence could continually favor the upward transport of moisture anomaly to moisten the tropospheric column and maintain the precipitation anomaly (Benedict and Randall 2007; Hsu and Li 2012; Wolding et al. 2017).

The increased horizontal moisture convergence anomaly was related to the enhancement of MJO-related convergence working on the mean moisture field $[-(\overline{q}\nabla \cdot V')]$. A further diagnosis was applied to quantify the relative contributions of thermodynamic effect (mean moisture change) and dynamic effect (circulation anomaly change). The results showed that the decadal change in the circulation anomaly $\overline{q}_1\Delta\delta'$ played a leading role, while the effects of mean moisture change $\Delta\overline{q}\delta_1'$ and its nonlinear interaction with circulation change $\Delta\overline{q}\Delta\delta'$ contributed insignificantly. This is in contrast to the mechanisms responsible for the MJO enhancement under future warming scenarios, in which the mean moisture change is the most important contributor but the circulation anomaly changes little (Chang et al. 2015; Wolding et al. 2017; Bui and Maloney 2018; Maloney et al. 2019). The difference in the key process accounting for increased moisture convergence and precipitation anomaly may be related to the competing effects between diabatic heating anomaly change and mean static stability change (Wolding et al. 2017; Bui and Maloney 2018; Cui and Li 2019). Under strong warming scenarios (such as RCP8.5), the atmosphere tends to be more stable, due to large increases in mean static stability. The changes in the MJO circulation anomaly in the twenty-first century are likely to either be negligible or exert a negative effect on precipitation anomaly enhancement. Thus, the major contributor to

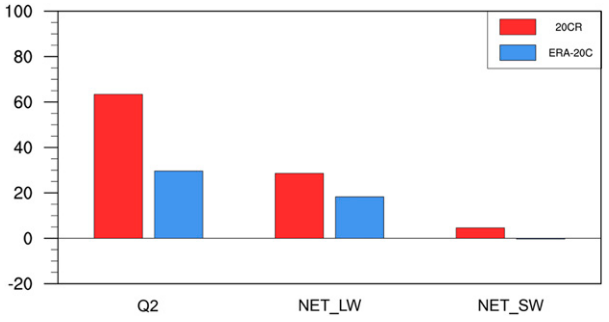

FIG. 13. As in Fig. 12b, but for changes in convective heating Q_2 ($W\,m^{-2}$) and radiative heating, including net longwave radiative heating (NET_LW; $W\,m^{-2}$) and net shortwave radiative heating (NET_SW; $W\,m^{-2}$) between D2 and D1 for 20CR (red bars) and ERA-20C (blue bars).

enhanced MJO precipitation amplitude is the mean moisture change (e.g., Chang et al. 2015; Adames et al. 2017; Wolding et al. 2017; Bui and Maloney 2018; Maloney et al. 2019; Rushley et al. 2019). In contrast, under the mild warming of the twentieth century, the increase in mean static stability was weak and its effect could not defeat the significant increases in latent and radiative heating anomalies. The enhanced circulation anomaly eventually dominated the enhanced moisture convergence anomaly, and resulted in the intensified MJO precipitation anomaly in the recent decadal period (D2).

In summary, an increase in the amplitude of MJO precipitation was found to accompany global warming. However, the extent of change in mean moisture and MJO circulation anomaly varies under different warming scenarios. Therefore, the mechanisms responsible for enhanced MJO precipitation amplitude are different for the twentieth-century warming and future projections. A recent study by Cui and Li (2019) found that the MJO circulation anomaly change during different warming phases under the RCP8.5 scenario can be controlled by the net effect of diabatic heating change and mean static stability change. The competing effect on circulation anomaly change is worthy of further study because the amplification of the circulation anomaly over the tropics can generate an enhanced teleconnection pattern and lead to a higher probability of extreme weather events in the middle to high latitudes (Cassou 2008; Stan et al. 2017). The mechanisms controlling the decadal change in MJO teleconnection were complex and involved various dynamic processes, including not only MJO-related perturbations but also the mean circulation and ocean states and their interactions (Baxter and Nigam 2013; Henderson et al. 2017; Lee et al. 2019). We will continue studying these issues.

Another issue worth of further in-depth studying is about the MJO change induced solely by nature variability. In the current study, we investigated the variation of MJO amplitude over the entire twentieth century under all nature and anthropogenic forcing combined. How and to what extent the different SST modes at the decadal-to-multidecadal time scales [such as the Atlantic multidecadal oscillation (AMO) and the Pacific decadal oscillation (PDO)] influence the MJO amplitude are our ongoing research. Our preliminary results revealed a close linkage between the weakening of boreal-winter MJO over the tropical Pacific and the warm phase of the AMO. Detailed processes explaining how the AMO affects the tropical Pacific MJO will be presented in the near future.

Acknowledgments. The authors thank the anonymous reviewers for their comments, which helped improve the manuscript. The authors also thank Dr. Compo and Dr. Mccoll for providing 20CRv2 data of individual members. This work was supported by the National Key Research and Development Program of China (2018YFC1505804).

REFERENCES

Adames, Á. F., D. Kim, A. H. Sobel, A. Del Genio, and J. Wu, 2017: Changes in the structure and propagation of the MJO with increasing CO_2. *J. Adv. Model. Earth Syst.*, **9**, 1251–1268, https://doi.org/10.1002/2017MS000913.

Arnold, N. P., M. Branson, Z. Kuang, D. A. Randall, and E. Tziperman, 2015: MJO intensification with warming in the superparameterized CESM. *J. Climate*, **28**, 2706–2724, https://doi.org/10.1175/JCLI-D-14-00494.1.

Baines, P. G., and C. K. Folland, 2007: Evidence for a rapid global climate shift across the late 1960s. *J. Climate*, **20**, 2721–2744, https://doi.org/10.1175/JCLI4177.1.

Baxter, S., and S. Nigam, 2013: A subseasonal teleconnection analysis: PNA development and its relationship to the NAO. *J. Climate*, **26**, 6733–6741, https://doi.org/10.1175/JCLI-D-12-00426.1.

Benedict, J. J., and D. A. Randall, 2007: Observed characteristics of the MJO relative to maximum rainfall. *J. Atmos. Sci.*, **64**, 2332–2354, https://doi.org/10.1175/JAS3968.1.

Bui, H. X., and E. D. Maloney, 2018: Changes in Madden–Julian oscillation precipitation and wind variance under global warming. *Geophys. Res. Lett.*, **45**, 7148–7155, https://doi.org/10.1029/2018GL078504.

——, and ——, 2019a: Transient response of MJO precipitation and circulation to greenhouse gas forcing. *Geophys. Res. Lett.*, **46**, 13 546–13 555, https://doi.org/10.1029/2019GL085328.

——, and ——, 2019b: Mechanisms for global warming impacts on Madden–Julian oscillation precipitation amplitude. *J. Climate*, **32**, 6961–6975, https://doi.org/10.1175/JCLI-D-19-0051.1.

Camargo, S. J., M. C. Wheeler, and A. H. Sobel, 2009: Diagnosis of the MJO modulation of tropical cyclogenesis using an empirical index. *J. Atmos. Sci.*, **66**, 3061–3074, https://doi.org/10.1175/2009JAS3101.1.

Carvalho, L. M., C. Jones, and B. Liebmann, 2004: The South Atlantic convergence zone: Intensity, form, persistence, and relationships with intraseasonal to interannual activity and extreme rainfall. *J. Climate*, **17**, 88–108, https://doi.org/10.1175/1520-0442(2004)017<0088:TSACZI>2.0.CO;2.

Cassou, C., 2008: Intraseasonal interaction between the Madden–Julian oscillation and the North Atlantic Oscillation. *Nature*, **455**, 523–527, https://doi.org/10.1038/nature07286.

Chang, C. W. J., W. L. Tseng, H. H. Hsu, N. Keenlyside, and B. J. Tsuang, 2015: The Madden–Julian oscillation in a warmer world. *Geophys. Res. Lett.*, **42**, 6034–6042, https://doi.org/10.1002/2015GL065095.

Chen, X., J. Ling, and C. Li, 2016: Evolution of the Madden–Julian oscillation in two types of El Niño. *J. Climate*, **29**, 1919–1934, https://doi.org/10.1175/JCLI-D-15-0486.1.

Compo, G. P., and Coauthors, 2011: The Twentieth Century Reanalysis Project. *Quart. J. Roy. Meteor. Soc.*, **137** (654), 1–28, https://doi.org/10.1002/qj.776.

Cui, J., and T. Li, 2019: Changes of MJO propagation characteristics under global warming. *Climate Dyn.*, **53**, 5311–5327, https://doi.org/10.1007/s00382-019-04864-4.

——, L. Wang, T. Li, and B. Wu, 2019: Can reanalysis products with only surface variables assimilated capture Madden–Julian oscillation characteristics? *Int. J. Climatol.*, **40**, 1279–1293, https://doi.org/10.1002/joc.6270.

Dee, D. P., and Coauthors, 2011: The ERA-Interim reanalysis: Configuration and performance of the data assimilation system. *Quart. J. Roy. Meteor. Soc.*, **137**, 553–597, https://doi.org/10.1002/qj.828.

Duchon, C. E., 1979: Lanczos filtering in one and two dimensions. *J. Appl. Meteor.*, **18**, 1016–1022, https://doi.org/10.1175/1520-0450(1979)018<1016:LFIOAT>2.0.CO;2.

Fu, X., J. Y. Lee, P. C. Hsu, H. Taniguchi, B. Wang, W. Wang, and S. Weaver, 2013: Multi-model MJO forecasting during DYNAMO/CINDY period. *Climate Dyn.*, **41**, 1067–1081, https://doi.org/10.1007/s00382-013-1859-9.

Gao, Y., P. C. Hsu, and H. H. Hsu, 2016: Assessments of surface latent heat flux associated with the Madden–Julian oscillation in reanalyses. *Climate Dyn.*, **47**, 1755–1774, https://doi.org/10.1007/s00382-015-2931-4.

Giese, B. S., H. F. Seidel, G. P. Compo, and P. D. Sardeshmukh, 2016: An ensemble of ocean reanalyses for 1815–2013 with sparse observational input. *J. Geophys. Res. Oceans*, **121**, 6891–6910, https://doi.org/10.1002/2016JC012079.

Goswami, B. N., and R. A. Mohan, 2001: Intraseasonal oscillations and interannual variability of the Indian summer monsoon. *J. Climate*, **14**, 1180–1198, https://doi.org/10.1175/1520-0442(2001)014<1180:IOAIVO>2.0.CO;2.

Henderson, S. A., E. D. Maloney, and S. Son, 2017: Madden–Julian oscillation Pacific teleconnections: The impact of the basic state and MJO representation in general circulation models. *J. Climate*, **30**, 4567–4587, https://doi.org/10.1175/JCLI-D-16-0789.1.

Hendon, H. H., and B. Liebmann, 1994: Organization of convection within the Madden–Julian oscillation. *J. Geophys. Res.*, **99**, 8073–8083, https://doi.org/10.1029/94JD00045.

——, ——, and J. D. Glick, 1998: Oceanic Kelvin waves and the Madden–Julian oscillation. *J. Atmos. Sci.*, **55**, 88–101, https://doi.org/10.1175/1520-0469(1998)055<0088:OKWATM>2.0.CO;2.

Hsu, P. C., and T. Li, 2012: Role of the boundary layer moisture asymmetry in causing the eastward propagation of the Madden–Julian oscillation. *J. Climate*, **25**, 4914–4931, https://doi.org/10.1175/JCLI-D-11-00310.1.

——, and T. Xiao, 2017: Differences in the initiation and development of the Madden–Julian oscillation over the Indian Ocean associated with two types of El Niño. *J. Climate*, **30**, 1397–1415, https://doi.org/10.1175/JCLI-D-16-0336.1.

Jiang, X., and Coauthors, 2011: Vertical diabatic heating structure of the MJO: Intercomparison between recent reanalyses and TRMM estimates. *Mon. Wea. Rev.*, **139**, 3208–3223, https://doi.org/10.1175/2011MWR3636.1.

——, and Coauthors, 2015: Vertical structure and physical processes of the Madden–Julian oscillation: Exploring key model physics in climate simulations. *J. Geophys. Res. Atmos.*, **120**, 4718–4748, https://doi.org/10.1002/2014JD022375.

Jones, C., and L. M. Carvalho, 2006: Changes in the activity of the Madden–Julian oscillation during 1958–2004. *J. Climate*, **19**, 6353–6370, https://doi.org/10.1175/JCLI3972.1.

Kalnay, E., and Coauthors, 1996: The NCEP/NCAR 40-Year Reanalysis Project. *Bull. Amer. Meteor. Soc.*, **77**, 437–471, https://doi.org/10.1175/1520-0477(1996)077<0437:TNYRP>2.0.CO;2.

Kanamitsu, M., W. Ebisuzaki, J. Woollen, S.-K. Yang, J. J. Hnilo, M. Fiorino, and G. L. Potter, 2002: NCEP–DOE AMIP-II Reanalysis (R-2). *Bull. Amer. Meteor. Soc.*, **83**, 1631–1643, https://doi.org/10.1175/BAMS-83-11-1631.

Kessler, W. S., 2001: EOF representation of the Madden–Julian oscillation and its connection with ENSO. *J. Climate*, **14**, 3055–3061, https://doi.org/10.1175/1520-0442(2001)014<3055:EROTMJ>2.0.CO;2.

Kim, D., A. H. Sobel, E. D. Maloney, D. M. Frierson, and I. S. Kang, 2011: A systematic relationship between intraseasonal variability and mean state bias in AGCM simulations. *J. Climate*, **24**, 5506–5520, https://doi.org/10.1175/2011JCLI4177.1.

Klingaman, N. P., X. Jiang, P. K. Xavier, J. Petch, D. Waliser, and S. J. Woolnough, 2015: Vertical structure and physical processes of the Madden–Julian oscillation: Synthesis and summary. *J. Geophys. Res. Atmos.*, **120**, 4671–4689, https://doi.org/10.1002/2015JD023196.

Lee, R. W., S. J. Woolnough, A. J. Charlton-Perez, and F. Vitart, 2019: ENSO modulation of MJO teleconnections to the North Atlantic and Europe. *Geophys. Res. Lett.*, **46**, 13 535–13 545, https://doi.org/10.1029/2019GL084683.

Lengaigne, M., E. Guilyardi, J. P. Boulanger, C. Menkes, P. Delecluse, P. Inness, J. Cole, and J. Slingo, 2004: Triggering of El Niño by westerly wind events in a coupled general circulation model. *Climate Dyn.*, **23**, 601–620, https://doi.org/10.1007/s00382-004-0457-2.

Liebmann, B., and C. A. Smith, 1996: Description of a complete (interpolated) outgoing longwave radiation dataset. *Bull. Amer. Meteor. Soc.*, **77**, 1275–1277, http://www.jstor.org/stable/26233278.

Lin, H., G. Brunet, and R. Mo, 2010: Impact of the Madden–Julian oscillation on wintertime precipitation in Canada. *Mon. Wea. Rev.*, **138**, 3822–3839, https://doi.org/10.1175/2010MWR3363.1.

Lin, J. L., and B. E. Mapes, 2004: Radiation budget of the tropical intraseasonal oscillation. *J. Atmos. Sci.*, **61**, 2050–2062, https://doi.org/10.1175/1520-0469(2004)061<2050:RBOTTI>2.0.CO;2.

Ling, J., C. Li, W. Zhou, X. Jia, and C. Zhang, 2013: Effect of boundary layer latent heating on MJO simulations. *Adv. Atmos. Sci.*, **30**, 101–115, https://doi.org/10.1007/s00376-012-2031-x.

——, Y. Zhao, and G. Chen, 2019: Barrier effect on MJO propagation by the maritime continent in the MJO task force/GEWEX atmospheric system study models. *J. Climate*, **32**, 5529–5547, https://doi.org/10.1175/JCLI-D-18-0870.1.

Liu, P., T. Li, B. Wang, M. Zhang, J. J. Luo, Y. Masumoto, X. Wang, and E. Roeckner, 2013: MJO change with A1B global warming estimated by the 40-km ECHAM5. *Climate Dyn.*, **41**, 1009–1023, https://doi.org/10.1007/s00382-012-1532-8.

Lorenz, D. J., and D. L. Hartmann, 2006: The effect of the MJO on the North American monsoon. *J. Climate*, **19**, 333–343, https://doi.org/10.1175/JCLI3684.1.

Lyu, M., X. Jiang, and Z. Wu, 2019: A cautionary note on the long-term trend in activity of the Madden–Julian oscillation during the past decades. *Geophys. Res. Lett.*, **46**, 14 063–14 071, https://doi.org/10.1029/2019GL086133.

Madden, R. A., and P. R. Julian, 1971: Detection of a 40–50 day oscillation in the zonal wind in the tropical Pacific. *J. Atmos. Sci.*, **28**, 702–708, https://doi.org/10.1175/1520-0469(1971)028<0702:DOADOI>2.0.CO;2.

——, and ——, 1972: Description of global-scale circulation cells in the tropics with a 40–50 day period. *J. Atmos. Sci.*, **29**, 1109–1123, https://doi.org/10.1175/1520-0469(1972)029<1109:DOGSCC>2.0.CO;2.

——, and ——, 1994: Observations of the 40–50-day tropical oscillation—A review. *Mon. Wea. Rev.*, **122**, 814–837, https://doi.org/10.1175/1520-0493(1994)122<0814:OOTDTO>2.0.CO;2.

Maloney, E. D., and S. P. Xie, 2013: Sensitivity of tropical intraseasonal variability to the pattern of climate warming. *J. Adv. Model. Earth Syst.*, **5**, 32–47, https://doi.org/10.1029/2012MS000171.

——, Á. F. Adames, and H. X. Bui, 2019: Madden–Julian oscillation changes under anthropogenic warming. *Nat. Climate Change*, **9**, 26–33, https://doi.org/10.1038/s41558-018-0331-6.

Oliver, E. C. J., and K. R. Thompson, 2012: A reconstruction of Madden–Julian oscillation variability from 1905 to 2008. *J. Climate*, **25**, 1996–2019, https://doi.org/10.1175/JCLI-D-11-00154.1.

Pohl, B., S. Janicot, B. Fontaine, and R. Marteau, 2009: Implication of the Madden–Julian oscillation in the 40-day variability of the West African monsoon. *J. Climate*, **22**, 3769–3785, https://doi.org/10.1175/2009JCLI2805.1.

Poli, P., and Coauthors, 2016: ERA-20C: An atmospheric reanalysis of the twentieth century. *J. Climate*, **29**, 4083–4097, https://doi.org/10.1175/JCLI-D-15-0556.1.

Rienecker, M. M., and Coauthors, 2011: MERRA: NASA's Modern-Era Retrospective Analysis for Research and Applications. *J. Climate*, **24**, 3624–3648, https://doi.org/10.1175/JCLI-D-11-00015.1.

Roxy, M. K., P. Dasgupta, M. J. McPhaden, T. Suematsu, C. Zhang, and D. Kim, 2019: Twofold expansion of the Indo-Pacific warm pool warps the MJO life cycle. *Nature*, **575**, 647–651, https://doi.org/10.1038/s41586-019-1764-4.

Rushley, S. S., D. Kim, and Á. F. Adames, 2019: Changes in the MJO under greenhouse gas–induced warming in CMIP5 models. *J. Climate*, **32**, 803–821, https://doi.org/10.1175/JCLI-D-18-0437.1.

Saha, S., and Coauthors, 2010: The NCEP Climate Forecast System Reanalysis. *Bull. Amer. Meteor. Soc.*, **91**, 1015–1057, https://doi.org/10.1175/2010BAMS3001.1.

Salby, M. L., R. R. Garcia, and H. H. Hendon, 1994: Planetary-scale circulations in the presence of climatological and wave-induced heating. *J. Atmos. Sci.*, **51**, 2344–2367, https://doi.org/10.1175/1520-0469(1994)051<2344:PSCITP>2.0.CO;2.

Singh, M. S., and P. A. O'Gorman, 2012: Upward shift of the atmospheric general circulation under global warming: Theory and simulations. *J. Climate*, **25**, 8259–8276, https://doi.org/10.1175/JCLI-D-11-00699.1.

Slingo, J. M., D. P. Rowell, K. R. Sperber, and F. Nortley, 1999: On the predictability of the interannual behaviour of the Madden–Julian oscillation and its relationship with El Niño. *Quart. J. Roy. Meteor. Soc.*, **125**, 583–609, https://doi.org/10.1256/SMSQJ.55410.

Sobel, A. H., and E. Maloney, 2013: Moisture modes and the eastward propagation of the MJO. *J. Atmos. Sci.*, **70**, 187–192, https://doi.org/10.1175/JAS-D-12-0189.1.

——, J. Nilsson, and L. M. Polvani, 2001: The weak temperature gradient approximation and balanced tropical moisture waves. *J. Atmos. Sci.*, **58**, 3650–3665, https://doi.org/10.1175/1520-0469(2001)058<3650:TWTGAA>2.0.CO;2.

Stan, C., D. M. Straus, J. S. Frederiksen, H. Lin, E. D. Maloney, and C. Schumacher, 2017: Review of tropical–extratropical teleconnections on intraseasonal time scales. *Rev. Geophys.*, **55**, 902–937, https://doi.org/10.1002/2016RG000538.

Subramanian, A., M. Jochum, A. J. Miller, R. Neale, H. Seo, D. Waliser, and R. Murtugudde, 2014: The MJO and global warming: A study in CCSM4. *Climate Dyn.*, **42**, 2019–2031, https://doi.org/10.1007/s00382-013-1846-1.

Titchner, H. A., and N. A. Rayner, 2014: The Met Office Hadley Centre sea ice and sea surface temperature data set, version 2:1. Sea ice concentrations. *J. Geophys. Res. Atmos.*, **119**, 2864–2889, https://doi.org/10.1002/2013JD020316.

Vitart, F., and F. Molteni, 2010: Simulation of the Madden–Julian oscillation and its teleconnections in the ECMWF forecast system. *Quart. J. Roy. Meteor. Soc.*, **136**, 842–855, https://doi.org/10.1002/qj.623.

Waliser, D., and Coauthors, 2009: MJO simulation diagnostics. *J. Climate*, **22**, 3006–3030, https://doi.org/10.1175/2008JCLI2731.1.

Wheeler, M. C., and H. H. Hendon, 2004: An all-season real-time multivariate MJO index: Development of an index for monitoring and prediction. *Mon. Wea. Rev.*, **132**, 1917–1932, https://doi.org/10.1175/1520-0493(2004)132<1917:AARMMI>2.0.CO;2.

Wolding, B. O., E. D. Maloney, S. Henderson, and M. Branson, 2017: Climate change and the Madden–Julian oscillation: A vertically resolved weak temperature gradient analysis. *J. Adv. Model. Earth Syst.*, **9**, 307–331, https://doi.org/10.1002/2016MS000843.

Yanai, M., S. Esbensen, and J. H. Chu, 1973: Determination of bulk properties of tropical cloud clusters from large-scale heat and moisture budgets. *J. Atmos. Sci.*, **30**, 611–627, https://doi.org/10.1175/1520-0469(1973)030<0611:DOBPOT>2.0.CO;2.

Zavala-Garay, J., C. Zhang, A. M. Moore, and R. Kleeman, 2005: The linear response of ENSO to the Madden–Julian oscillation. *J. Climate*, **18**, 2441–2459, https://doi.org/10.1175/JCLI3408.1.

Zelinka, M. D., and D. L. Hartmann, 2011: The observed sensitivity of high clouds to mean surface temperature anomalies in the tropics. *J. Geophys. Res.*, **116**, D23103, https://doi.org/10.1029/2011JD016459.

Zhang, C., 2005: Madden–Julian oscillation. *Rev. Geophys.*, **43**, RG2003, https://doi.org/10.1029/2004RG000158.

——, and M. Dong, 2004: Seasonality in the Madden–Julian oscillation. *J. Climate*, **17**, 3169–3180, https://doi.org/10.1175/1520-0442(2004)017<3169:SITMO>2.0.CO;2.

——, J. Gottschalck, E. D. Maloney, M. W. Moncrieff, F. Vitart, D. E. Waliser, B. Wang, and M. C. Wheeler, 2013: Cracking the MJO nut. *Geophys. Res. Lett.*, **40**, 1223–1230, https://doi.org/10.1002/grl.50244.